Research Article | Vol. 25, No. 21 | 16 Oct 2017 | OPTICS EXPRESS 25023
Optics EXPRESS

Miniature all-optical probe for large synthetic aperture photoacoustic-ultrasound imaging

GUANGYAO LI,[1] ZHENDONG GUO,[1] AND SUNG-LIANG CHEN[1,2,*]

[1]*University of Michigan-Shanghai Jiao Tong University Joint Institute, Shanghai Jiao Tong University, Shanghai 200240, China*
[2]*State Key Laboratory of Advanced Optical Communication Systems and Networks, Shanghai Jiao Tong University, Shanghai 200240, China*
**sungliang.chen@sjtu.edu.cn*

Abstract: A miniature all-optical probe for high-resolution photoacoustic (PA)-ultrasound (US) imaging using a large synthetic aperture is developed. The probe consists of three optical fibers for PA excitation, US generation, and detection of acoustic waves, respectively. The fiber for PA excitation has a large numerical aperture (NA) for wide-angle laser illumination. On the other hand, the fiber with a carbon black-polydimethylsiloxane composite coated on the end face of the optical fiber is used for wide-angle US transmission through laser-US conversion. Both the excited PA and backscattered US signals are detected by a fiber-tip Fabry-Perot cavity for wide-angle acoustic detection. The probe outer diameter is only ~2 mm. The synergy of the three optical fibers makes a large-NA synthetic aperture focusing technique for high-resolution PA and US imaging possible. High PA lateral resolutions of 104–154 μm and high US lateral resolutions of 64–112 μm over a depth range of > 4 mm are obtained. Compared with other existing miniature PA-US probes, to our knowledge, our probe achieves by far the best performance in terms of lateral resolutions and imaging depth range. The constructed probe has potential for endoscopic and intravascular imaging applications that require PA and US contrasts with high resolutions over a large depth range.

OCIS codes: (170.5120) Photoacoustic imaging; (170.7170) Ultrasound; (120.2230) Fabry-Perot.

References and links

1. S. Jiao, M. Jiang, J. Hu, A. Fawzi, Q. Zhou, K. K. Shung, C. A. Puliafito, and H. F. Zhang, "Photoacoustic ophthalmoscopy for in vivo retinal imaging," Opt. Express **18**(4), 3967–3972 (2010).
2. A. Nair, B. D. Kuban, E. M. Tuzcu, P. Schoenhagen, S. E. Nissen, and D. G. Vince, "Coronary plaque classification with intravascular ultrasound radiofrequency data analysis," Circulation **106**(17), 2200–2206 (2002).
3. K. Jansen, A. F. W. van der Steen, H. M. M. van Beusekom, J. W. Oosterhuis, and G. van Soest, "Intravascular photoacoustic imaging of human coronary atherosclerosis," Opt. Lett. **36**(5), 597–599 (2011).
4. J. Mamou, O. Aristizábal, R. H. Silverman, J. A. Ketterling, and D. H. Turnbull, "High-frequency chirp ultrasound imaging with an annular array for ophthalmologic and small-animal imaging," Ultrasound Med. Biol. **35**(7), 1198–1208 (2009).
5. J. Xia and L. V. Wang, "Small-animal whole-body photoacoustic tomography: a review," IEEE Trans. Biomed. Eng. **61**(5), 1380–1389 (2014).
6. R. Nuster, N. Schmitner, G. Wurzinger, S. Gratt, W. Salvenmoser, D. Meyer, and G. Paltauf, "Hybrid photoacoustic and ultrasound section imaging with optical ultrasound detection," J. Biophotonics **6**(6-7), 549–559 (2013).
7. K. Daoudi, P. J. van den Berg, O. Rabot, A. Kohl, S. Tisserand, P. Brands, and W. Steenbergen, "Handheld probe integrating laser diode and ultrasound transducer array for ultrasound/photoacoustic dual modality imaging," Opt. Express **22**(21), 26365–26374 (2014).
8. P. Subochev, A. Orlova, M. Shirmanova, A. Postnikova, and I. Turchin, "Simultaneous photoacoustic and optically mediated ultrasound microscopy: an in vivo study," Biomed. Opt. Express **6**(2), 631–638 (2015).
9. S.-Y. Hung, W.-S. Wu, B.-Y. Hsieh, and P.-C. Li, "Concurrent photoacoustic-ultrasound imaging using single-laser pulses," J. Biomed. Opt. **20**(8), 86004 (2015).
10. X. Bai, X. Gong, W. Hau, R. Lin, J. Zheng, C. Liu, C. Zeng, X. Zou, H. Zheng, and L. Song, "Intravascular optical-resolution photoacoustic tomography with a 1.1 mm diameter catheter," PLoS One **9**(3), e92463 (2014).

#305842 https://doi.org/10.1364/OE.25.025023
Journal © 2017 Received 29 Aug 2017; revised 25 Sep 2017; accepted 25 Sep 2017; published 2 Oct 2017

Optics EXPRESS

11. D. VanderLaan, A. B. Karpiouk, D. Yeager, and S. Emelianov, "Real-time intravascular ultrasound and photoacoustic imaging," IEEE Trans. Ultrason. Ferroelectr. Freq. Control **64**(1), 141–149 (2017).
12. S. Sethuraman, J. H. Amirian, S. H. Litovsky, R. W. Smalling, and S. Y. Emelianov, "Ex vivo characterization of atherosclerosis using intravascular photoacoustic imaging," Opt. Express **15**(25), 16657–16666 (2007).
13. S. Sethuraman, S. R. Aglyamov, J. H. Amirian, R. W. Smalling, and S. Y. Emelianov, "Intravascular photoacoustic imaging using an IVUS imaging catheter," IEEE Trans. Ultrason. Ferroelectr. Freq. Control **54**(5), 978–986 (2007).
14. B. Wang, J. L. Su, J. Amirian, S. H. Litovsky, R. Smalling, and S. Emelianov, "Detection of lipid in atherosclerotic vessels using ultrasound-guided spectroscopic intravascular photoacoustic imaging," Opt. Express **18**(5), 4889–4897 (2010).
15. B.-Y. Hsieh, S.-L. Chen, T. Ling, L. J. Guo, and P.-C. Li, "Integrated intravascular ultrasound and photoacoustic imaging scan head," Opt. Lett. **35**(17), 2892–2894 (2010).
16. A. B. Karpiouk, B. Wang, and S. Y. Emelianov, "Development of a catheter for combined intravascular ultrasound and photoacoustic imaging," Rev. Sci. Instrum. **81**(1), 014901 (2010).
17. W. Wei, X. Li, Q. Zhou, K. K. Shung, and Z. Chen, "Integrated ultrasound and photoacoustic probe for co-registered intravascular imaging," J. Biomed. Opt. **16**(10), 106001 (2011).
18. R. J. Colchester, E. Z. Zhang, C. A. Mosse, P. C. Beard, I. Papakonstantinou, and A. E. Desjardins, "Broadband miniature optical ultrasound probe for high resolution vascular tissue imaging," Biomed. Opt. Express **6**(4), 1502–1511 (2015).
19. B.-Y. Hsieh, S.-L. Chen, T. Ling, L. J. Guo, and P.-C. Li, "All-optical transducer for ultrasound and photoacoustic imaging by dichroic filtering," in Ultrasonics Symposium (IUS, 2012), pp. 1410–1413.
20. B.-Y. Hsieh, S.-L. Chen, T. Ling, L. J. Guo, and P.-C. Li, "All-optical scanhead for ultrasound and photoacoustic imaging-Imaging mode switching by dichroic filtering," Photoacoustics **2**(1), 39–46 (2014).
21. R. J. Colchester, C. A. Mosse, D. I. Nikitichev, E. Z. Zhang, S. West, P. C. Beard, I. Papakonstantinou, and A. E. Desjardins, "Real-time needle guidance with photoacoustic and laser-generated ultrasound probes," Proc. SPIE **9323**, 932321 (2015).
22. W. Xia, C. A. Mosse, R. J. Colchester, J. M. Mari, D. I. Nikitichev, S. J. West, S. Ourselin, P. C. Beard, and A. E. Desjardins, "Fiber optic photoacoustic probe with ultrasonic tracking for guiding minimally invasive procedures," Proc. SPIE **9539**, 95390K (2015).
23. S.-L. Chen, L. J. Guo, and X. Wang, "All-optical photoacoustic microscopy," Photoacoustics **3**(4), 143–150 (2015).
24. S.-L. Chen, "Review of laser-generated ultrasound transmitters and their applications to all-optical ultrasound transducers and imaging," Appl. Sci. **7**(1), 25 (2017).
25. S.-W. Huang, S.-L. Chen, T. Ling, A. Maxwell, M. O'Donnell, L. J. Guo, and S. Ashkenazi, "Low-noise wideband ultrasound detection using polymer microring resonators," Appl. Phys. Lett. **92**(19), 193509 (2008).
26. S.-W. Huang, Y. Hou, S. Ashkenazi, and M. O'Donnell, "High-resolution ultrasonic imaging using an etalon detector array," Appl. Phys. Lett. **93**(11), 113501 (2008).
27. C. Zhang, T. Ling, S.-L. Chen, and L. J. Guo, "Ultrabroad bandwidth and highly sensitive optical ultrasonic detector for photoacoustic imaging," ACS Photonics **1**(11), 1093–1098 (2014).
28. P. Morris, A. Hurrell, A. Shaw, E. Zhang, and P. Beard, "A Fabry-Perot fiber-optic ultrasonic hydrophone for the simultaneous measurement of temperature and acoustic pressure," J. Acoust. Soc. Am. **125**(6), 3611–3622 (2009).
29. E. Z. Zhang and P. C. Beard, "A miniature all-optical photoacoustic imaging probe," Proc. SPIE **7899**, 78991F (2011).
30. E. Z. Zhang and P. C. Beard, "Characteristics of optimized fibre-optic ultrasound receivers for minimally invasive photoacoustic detection," Proc. SPIE **9323**, 932311 (2015).
31. T. J. Allen, E. Zhang, and P. C. Beard, "Large-field-of-view laser-scanning OR-PAM using a fibre optic sensor," Proc. SPIE **9323**, 93230Z (2015).
32. S.-L. Chen, Y.-C. Chang, C. Zhang, J. G. Ok, T. Ling, M. T. Mihnev, T. B. Norris, and L. J. Guo, "Efficient real-time detection of terahertz pulse radiation based on photoacoustic conversion by carbon nanotube nanocomposite," Nat. Photonics **8**, 537–542 (2014).
33. J. M. Cannata, J. A. Williams, Q. Zhou, T. A. Ritter, and K. K. Shung, "Development of a 35-MHz piezo-composite ultrasound array for medical imaging," IEEE Trans. Ultrason. Ferroelectr. Freq. Control **53**(1), 224–236 (2006).
34. M.-L. Li, W.-J. Guan, and P.-C. Li, "Improved synthetic aperture focusing technique with applications in high-frequency ultrasound imaging," IEEE Trans. Ultrason. Ferroelectr. Freq. Control **51**(1), 63–70 (2004).
35. C.-K. Liao, M.-L. Li, and P.-C. Li, "Optoacoustic imaging with synthetic aperture focusing and coherence weighting," Opt. Lett. **29**(21), 2506–2508 (2004).
36. D. Cai, Z. Li, Y. Li, Z. Guo, and S.-L. Chen, "Photoacoustic microscopy in vivo using synthetic-aperture focusing technique combined with three-dimensional deconvolution," Opt. Express **25**(2), 1421–1434 (2017).
37. D. Cai, G. Li, D. Xia, Z. Li, Z. Guo, and S.-L. Chen, "Synthetic aperture focusing technique for photoacoustic endoscopy," Opt. Express **25**(2), 20162–20171 (2017).
38. S.-L. Chen, S.-W. Huang, T. Ling, S. Ashkenazi, and L. J. Guo, "Polymer microring resonators for high-sensitivity and wideband photoacoustic imaging," IEEE Trans. Ultrason. Ferroelectr. Freq. Control **56**(11), 2482–2491 (2009).

Optics EXPRESS

39. J.-M. Yang, K. Maslov, H.-C. Yang, Q. Zhou, K. K. Shung, and L. V. Wang, "Photoacoustic endoscopy," Opt. Lett. **34**(10), 1591–1593 (2009).

1. Introduction

Photoacoustic (PA) imaging forms an image based on optical absorption contrast with ultrasound (US) resolutions. In contrast, US imaging is based on acoustic backscattering to provide structural information. Both PA and US imaging has been demonstrated in a variety of biomedical applications such as ophthalmology [1], intravascular imaging [2,3], and small-animal imaging [4,5]. The contrasts of PA and US imaging are complementary, which is useful to provide more comprehensive information. Because the two imaging modalities receive the same signal form, acoustic waves, a PA-US dual modality system can be implemented by sharing the same acoustic detector. As for signal generation, a pulsed laser is used for PA excitation in PA imaging, while either a piezoelectric transducer or laser-US conversion can be used for US transmission in US imaging. Particularly, fiber-optic laser-US generation is promising because it can easily generate broadband wide-angle US and is easy for miniaturization.

While PA-US dual modality systems have been demonstrated previously [6–9], there is a need to miniaturize the PA-US imaging probe for interventional applications [3,10,11]. In recent studies, it has been reported that intravascular PA (IVPA) and intravascular US (IVUS) imaging are useful for detecting atherosclerotic plaques [2,3,10–17]. Vulnerable plaques characterized by thin fibrous caps and lipid-rich cores pose a high rupture risk in the coronary arteries and may block the blood supply to the heart. IVPA imaging can be used to identify the plaques by visualizing the lipid based on its characteristic optical absorption, while IVUS is able to obtain the anatomical details of the plaques [13]. IVPA catheters were developed using a commercial IVUS catheter with external light illumination [12–14], which restricts their use for *in vivo* applications. Several miniature probes capable of PA-US imaging with internal light illumination were then proposed and demonstrated [3,10,11,15–17]. In all these works, piezoelectric transducers were used for US generation and acoustic detection (except [15]). When fabricating the PA-US probe, piezoelectric technology may have several issues such as complexity with fabricating the electrical probes, difficulty in miniaturization, size-dependent sensitivity, and limited bandwidth [18]. One way to circumvent these challenges is to implement the PA-US probe through an all-optical platform [19–24].

Laser-US conversion offers the unique advantage in broadband US generation via the PA effect. Briefly, a pulsed laser is absorbed by a material and is converted into heat, which leads to an instantaneous temperature rise of the material. Through thermoelastic effect, the temperature rise further results in propagation of pressure waves. Optical acoustic detection shares the same advantage in receiving broadband acoustic waves [25–27]. Moreover, the optical platform that employs optical fibers for US generation and acoustic detection enables miniaturization for minimally invasive use and low cost. Several approaches for optical acoustic detectors on the tip of an optical fiber have been reported, where a Fabry-Perot (FP) cavity is one promising method [28–31]. The fiber-tip FP cavity can provide high sensitivity, broad bandwidth over tens of MHz, and wide-angle detection [31]. An all-optical miniature US probe has been demonstrated for high-resolution vascular tissue imaging [18], yet PA imaging modality was not integrated. The laser for PA excitation can also be delivered through an optical fiber. Thus, when PA excitation, US transmission, acoustic detection are all realized based on optical fibers, such all-optical design allows a highly miniaturized PA-US imaging probe.

In this paper, we describe a novel miniature dual-modality PA-US imaging probe consisting of three optical fibers for PA excitation, US transmission, and acoustic detection, respectively, to achieve high resolutions over a large imaging depth range. Specifically, the highlight of this work is that compared with other existing miniature PA-US probes, to our knowledge, our probe achieves by far the best performance in terms of lateral resolutions and

Optics EXPRESS

imaging depth range. This is made possible by the distinctive probe design capable of wide-angle PA excitation, US transmission, and acoustic detection simultaneously for a large synthetic aperture PA and US imaging. The all-optical fiber-optic design enables a miniaturized PA-US probe with an outer diameter of ~2 mm. Moreover, it has the advantage of immunity against electromagnetic interference.

2. Methods

2.1 PA-US probe and imaging system

A 200-μm core multi-mode optical fiber (M44L02, Thorlabs) with a large numerical aperture (NA) of 0.5 is used for wide-angle PA excitation. A carbon black-polydimethylsiloxane (PDMS) thin film was coated on the tip of another 100-μm multi-mode optical fiber for wide-angle US transmission. To create the composite film, we first uniformly mixed the carbon black powder and PDMS. Then, the end face of the cleaved optical fiber was dip coated with the mixture and UV curing was subsequently applied. The film thickness and the weight ratio of carbon black and PDMS are 27 μm and 5:1, respectively. Taken with a microscope, the picture of the fabricated fiber-tip US transmitter is shown in Fig. 1(a). Acoustic detection is realized by the fiber-tip FP acoustic sensor. The photo of the constructed PA-US probe consisting of three optical fibers is shown in Fig. 1(b). The laser (Q-smart 450, Quantel Laser) with a wavelength of 532 nm, a pulse duration of ~6 ns, and a repetition rate of 20 Hz was coupled to the two fibers (PA excitation and US generation) using a beam splitter. In the experiment, we perform PA and US imaging modalities separately. That is, in each mode, the light is coupled to one fiber at a time by blocking the light to the other fiber, which avoids the problem that the excitation pulses reach the two fiber tips at approximately the same time, resulting in the issue of not being able to distinguish between PA and US waves detected by the same FP sensor. The alignment of coupling the laser into the fiber takes time. For convenience, the beam splitter is used to avoid doing the alignment every time when switching between PA and US modes. The laser energies coupled to the PA and US fibers were ~430 and ~42 μJ, respectively, for the experiments in Section 3. The imaging system for the PA-US probe is shown in Fig. 2. The probe was mounted on a motorized stage (PLS-85, Physik Instrumente (PI)) and will be scanned laterally during PA and US data acquisition.

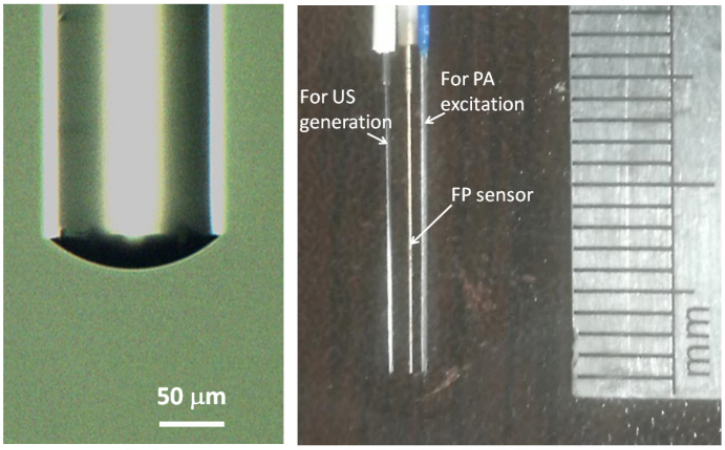

Fig. 1. (a) Picture of the fabricated fiber-tip US transmitter. (b) Photo of the constructed PA-US probe.

Optics EXPRESS

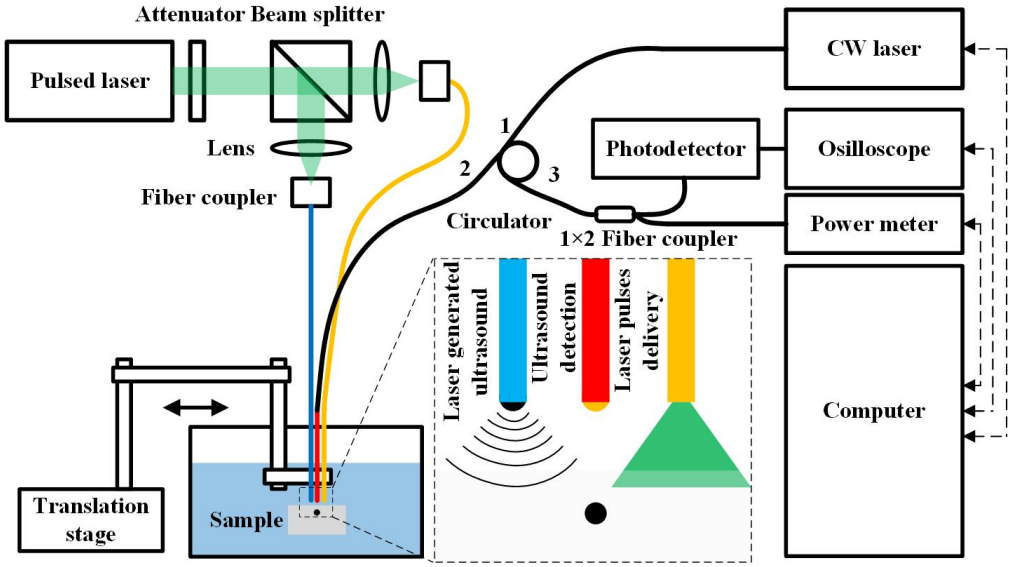

Fig. 2. Schematic of the integrated PA-US imaging system. Inset: schematic of the miniature PA-US probe.

Detection of acoustic waves is by using the fiber-tip FP acoustic sensor fabricated on the end face of a single mode optical fiber. The FP cavity comprises a polymer spacer sandwiched between two gold mirror coatings, which were deposited by sputtering. The first mirror was deposited onto the cleaved fiber end face, and the second one was on the surface of the polymer spacer. The reflectivities of the first and second mirrors were 81% and 98%, respectively. The spacer film with Young's modulus of ~4–5 GPa was dip coated by using a motorized stage and was thermally cured. The film thickness was measured as 20 μm. Finally, a Parylene-C film with a thickness of ~5 μm was coated for protection of the fiber-tip FP structure. The FP sensor was probed using a continuous wave tunable laser (HP 8168F, Agilent) with the wavelength range of 1450–1590 nm. The probing wavelength was selected at the wavelength with a high slope in the cavity reflection spectrum so that the FP sensor can be biased to provide high sensitivity from phase modulation due to incoming acoustic pressure into the amplitude modulation of the optical output power. Therefore, high quality (Q) factor leads to high sensitivity. A fiber circulator was used to access the input and output ports of the FP sensor. The output port collecting the reflected light was further connected to a 1 × 2 fiber coupler with a power ratio of 10:90. The 10% reflected power was measured by a power meter (2832-C, Newport) to obtain the FP cavity reflection spectrum, and the 90% power was detected using a photodetector (1811-FC-AC, New Focus) with an output gain of 4×10^4 V/A and electrical bandwidth of 25 kHz–125 MHz to record the fast-varying modulated optical power corresponding to the incident acoustic pressure. Figure 3(a) shows the measured FP reflection spectrum, where the free spectral range and the spectral width of the resonance dip can be determined to be 37 nm and ~2 nm, respectively. The Q factor can thus be estimated as ~750 [= 1507/2]. In experiments, we used a feedback control method to track the optimal probing wavelength of the FP sensor to ensure the stability of the detection sensitivity. The details of the method can be found in our previous work [32].

The FP sensitivity and noise-equivalent pressure (NEP) were calibrated using a 10 MHz unfocused US transducer (V312, Panametrics NDT, MA). The generated pressure of the transducer was ~45 kPa, which was calibrated using a commercial hydrophone (HGL-0085, ONDA). As shown in Fig. 3(b), the peak output voltage measured by the FP sensor is 172 mV under a 45-kPa acoustic pressure, and thus, the sensitivity of the FP sensor is determined to be ~3.8 mV/kPa. The root-mean-square noise level is 1.5 mV over 1–30 MHz bandwidth, and

Optics EXPRESS

thus, the corresponding NEP is estimated to be better than ~0.4 kPa over bandwidth of 29 MHz by extrapolating the sensitivity at 10 MHz to that over a wide frequency range (i.e., 1–30 MHz) based on the calibrated frequency response, as discussed later. The 10 MHz transducer has bandwidth of 7–13 MHz. The sensitivity of the ONDA hydrophone has an almost flat response (variations within 2 dB) in this frequency band (http://www.ondacorp.com/images/brochures/Onda_HGL_DataSheet.pdf). Thus, it is reasonable to assume a constant sensitivity of the ONDA hydrophone in this frequency band. In this calibration, the distance between the 10 MHz transducer and the ONDA hydrophone was ~2.3 mm, and the distance between the 10 MHz transducer and the FP sensor was kept approximately the same.

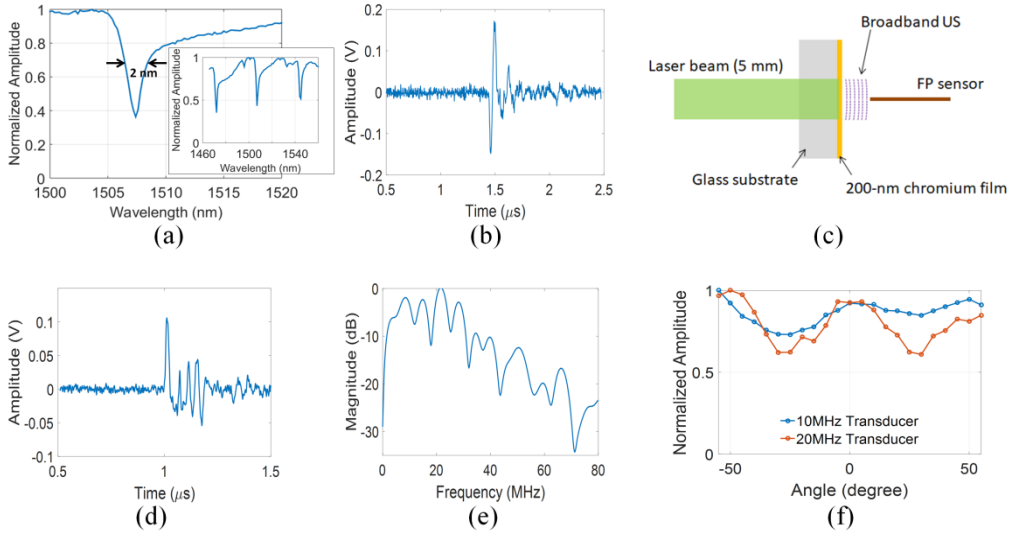

Fig. 3. FP sensor calibration. (a) FP reflection spectrum at a wavelength range of 1500–1520 nm; Inset: FP reflection spectrum over a wider wavelength range. (b) Sensitivity calibration: FP detected US signal generated by the unfocused US transducer. (c) Schematic of frequency response calibration. (d) Frequency response calibration: FP measured time-domain signal. (e) Frequency response calibration: estimated FP frequency response. (f) Measured FP angular response.

The detection bandwidth of the FP sensor was calibrated using a broadband optoacoustic source. By illuminating a 200-nm thick chromium film using a 6-ns pulsed laser with a spot size of 5 mm in diameter, a planar acoustic wave with a temporal profile duplicating that of the excitation laser pulse can be generated [25]. Figure 3(c) shows a schematic of the calibration. In this calibration, the majority of the laser was absorbed and reflected, and the light transmission was negligible considering a 200-nm thick chromium film. The chromium film was placed 1.5 mm from the FP sensor and the measured acoustic pulse is shown in Fig. 3(d). Figure 3(e) presents the estimated frequency response of the FP sensor by comparing the two spectra of the laser pulse and the measured acoustic pulse [25]. Note that the compensation for acoustic attenuation due to the sound coupling in water has been considered, which has an attenuation coefficient of 2.2×10^{-4} dB/mm MHz^2 [33]. The bandwidth of the sensor is estimated to be 29 MHz at −10 dB, although there is a narrow dip slightly lower than −10 dB at ~20 MHz. The non-uniformity in the frequency response arises from the sharp diffractive boundary of the plano-convex FP sensing cavity [30]. The angular response was calibrated using commercial 10 and 20 MHz flat US transducers to provide the acoustic source at different angles. The angular response is shown in Fig. 3(f). As can be seen, the FP sensor has very wide detection angle of more than ± 50° for 10 and 20 MHz acoustic sources. In Fig. 3(f), distinct variations of the angular response are observed, which

Optics EXPRESS

is also because of the sharp diffractive boundary of the plano-convex FP sensing cavity [30]. The rounded-tip design of the FP sensor can significantly reduce the edge wave components to improve the frequency and angular responses [30].

On the other hand, the US transmission angle from the tip of the 100-μm optical fiber was also measured using our FP sensor. In this measurement, the 100-μm optical fiber was kept stationary while the FP sensor was rotated at different angles with the tip of the 100-μm optical fiber as the rotation center. As shown in Fig. 4(a), the transmission angle can be more than ± 50°. Moreover, we characterized the US pressure and bandwidth of the fiber-tip US transmitter using the ONDA hydrophone (± 3 dB bandwidth: 0.25–40 MHz). The ONDA hydrophone was axially aligned with the fiber-tip US transmitter at a distance of ~2 mm, as shown in Fig. 4(b). Figures 4(c) and 4(d) show the PA A-line signal and its spectrum, respectively, which indicates a pressure level of ~150 kPa and −10-dB bandwidth of ~21 MHz of our fiber-tip US transmitter. Broader bandwidth may be achieved by using a smaller-core optical fiber and a thinner absorber. The laser pulse energy used in this measurement was 6 μJ per pulse, so that the fluence at the fiber end face was 76.4 mJ/cm^2. The wide-angle US transmission (Fig. 4(a)) and acoustic detection (Fig. 3(f)) enable a large synthetic aperture for high-resolution US imaging, while the wide-angle PA excitation and the same wide-angle acoustic detection allow a large synthetic aperture for high-resolution PA imaging.

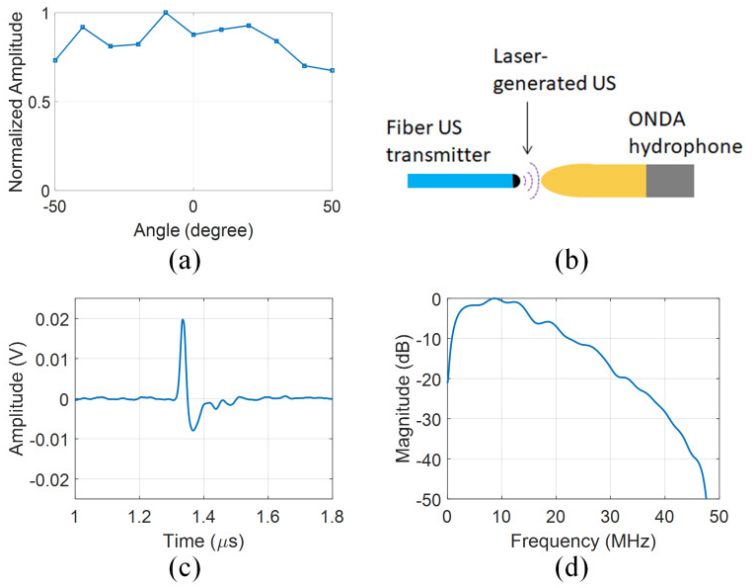

Fig. 4. Fiber US transmitter calibration. (a) Measured transmission angle of the fiber US transmitter. (b) Schematic of US pressure measurement by the ONDA hydrophone. (c) Time-domain signal measured by the ONDA hydrophone for acoustic pressure calibration. (d) Spectrum of (c)

2.2 Signal and image processing

Besides the backscattered US signals, the FP sensor also collects the acoustic signals propagated directly from the US transmitter at the fiber tip. Thus, crosstalk image artifacts are presented in B-mode images, as shown in Fig. 5(a). We perform signal processing to remove the artifacts prior to image reconstruction. The method of the crosstalk removal can be found in [18]. Figure 5(b) shows the B-mode image after applying the crosstalk removal signal processing to Fig. 5(a). Figures 5(c) and 5(d) show the images zoom into the region of crosstalk in Figs. 5(a) and 5(b), respectively. As can be seen, the crosstalk signals can be perfectly removed.

Optics EXPRESS

By scanning the miniature probe, a large aperture can be synthesized. The high-resolution PA and US images can be formed by synthetic aperture focusing technique (SAFT) reported previously [20,34–37]. Briefly, this is based on the standard delay-and-sum operation in the time domain for beam focusing to provide high lateral resolutions. Assuming the probe is linearly scanned, for a specific depth profile, the signals obtained at different sensor positions are delayed to a corresponding reference point and then summed coherently. The algorithms for PA SAFT and US SAFT are similar, and the main difference is that the applied delayed time in PA SAFT follows a one-way scheme while that in US SAFT takes a round-trip scheme. Finally, the PA and US images can be fused to display a dual-modality image. In the SAFT algorithm used in this work, coherence factor is also applied to further improve resolution and signal-to-noise ratios (SNRs). Note that the lateral position shift of the fibers, as shown in Fig. 1(b), is taken into account in the SAFT algorithm, which facilitates PA and US image coregistration. In this regard, it is relatively easy to estimate the lateral position shift of the fibers by placing them in a line, as shown in Fig. 1(b). A triangular placement of the three fibers can further reduce the probe size.

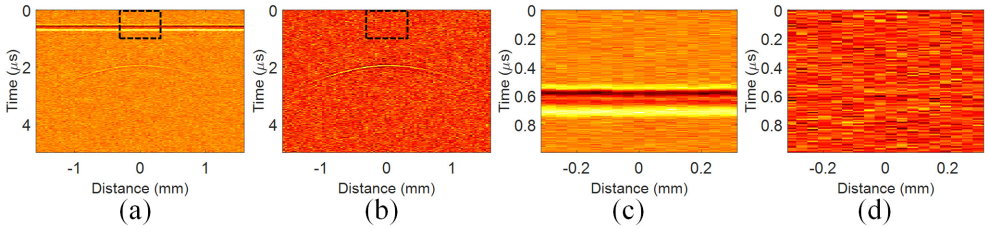

Fig. 5. (a) B-mode images before applying the crosstalk removal signal processing. (b) B-mode images after applying the crosstalk removal signal processing to (a). (c) The zoom image of the dashed box in (a). (d) The zoom image of the dashed box in (b).

3. Results

3.1 Spatial resolution and imaging depth range

To calibrate the lateral resolutions of the dual-modality imaging probe, 90-μm human hairs and 125-μm glass fibers placed at five different depths at 1–5 mm were imaged by PA and US modes, respectively. As mentioned previously, the crosstalk removal algorithm is applied to the raw signals to make the PA and US signals prominent. After applying SAFT and Hilbert transform (envelope detection) along the depth direction, the objects are clearly visualized in PA and US images, as shown in Figs. 6(a) and 6(b), respectively. We use the images to estimate resolutions. Figures 6(c) and 6(d) illustrate resolutions determined by the image at representative depth of 2 mm. One-dimensional lateral and axial profiles through the peak of the image and their Gaussian fits are checked. Then, the resolution can be determined by the full width at half maximum of the Gaussian curve. Using this method, we can estimate the lateral and axial resolutions at different depths, as shown in Fig. 6(e). The calibrated PA and US lateral resolutions are 104–154 μm and 64–112 μm, respectively, over a depth range of 4 mm. The high PA lateral resolutions after SAFT are attributed to the large-NA laser illumination using the large-NA optical fiber and the wide-angle acoustic detection of the FP sensor. On the other hand, the high US lateral resolutions after SAFT are realized by virtual of the wide-angle US transmission through laser-US generation of a small source and the same wide-angle acoustic detection of the FP sensor. On the other hand, the PA and US axial resolutions are 72–117 μm and 31–67 μm, respectively, over a depth range of 4 mm.

Optics EXPRESS

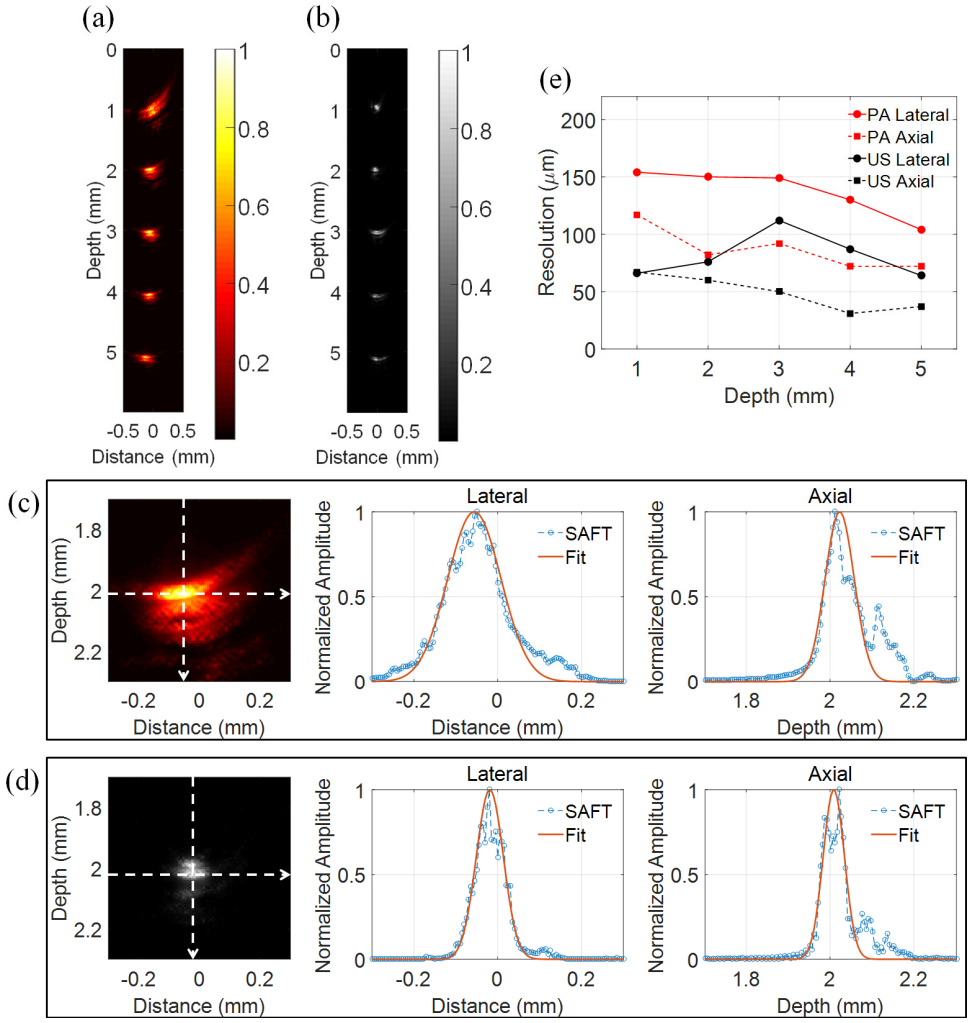

Fig. 6. (a) PA image of 90-μm human hairs at depths of 1–5 mm. (b) US image of 125-μm glass fibers at depths of 1–5 mm. (c) PA resolutions determined by the image at representative depth of 2 mm. (d) US resolutions determined by the image at representative depth of 2 mm. (e) PA and US spatial resolutions at different depths.

US lateral resolutions at different depths are similar except at depth of 3 mm, while PA lateral resolutions become better as imaging depth increases. This can be explained as follows. In PA modality, the size of the synthetic aperture is determined by the overlap of the laser illumination pattern and the acoustic detection pattern, while in US modality, that is determined by the overlap of the US generation pattern and the acoustic detection pattern. The acoustic detection pattern is the same for both modalities by using the same FP sensor, while the laser illumination pattern (NA: 0.5) in PA modality is relatively narrower than the US generation pattern (Fig. 4(a)) in US modality. Thus, a lateral separation of the two fibers for PA modality results in a more asymmetric and smaller-NA synthetic aperture for objects (i.e., worse resolutions) at shallow depths compared with objects at deep depths, while a lateral separation of the two fibers for US modality does not affect the images at different depths much. This is also evidenced by the imaged target at depth of 1 mm in Fig. 6(a), where we observe a high asymmetry and large lateral extent due to the asymmetric and small-NA synthetic aperture in PA SAFT reconstruction, while the phenomenon is not observed in the

Optics EXPRESS

US counterpart. That is, PA images will be degraded if the samples are placed closer to the probe. A small distance between the two fibers for PA modality is helpful to alleviate the issue, which is possible by removing the coatings of the fibers.

Although the FP sensor with a very low NEP of 8 Pa over bandwidth of 20 MHz was reported [29], our home-built FP sensor currently achieves a moderate NEP of ~0.4 kPa (i.e., 50 times worse). To show both high resolutions and a large imaging depth range, we use relatively large targets to have SNRs of images, especially for deep targets. It is possible to improve the sensitivity of the current fiber FP sensor by up to 50 times by referring to the reported result (NEP: 8 Pa) [29]. In this regard, the ultimate resolutions can be measured by imaging small objects. The ultimate resolutions might be better than the quoted values above, although further calibration is needed.

3.2 Two-dimensional phantom imaging

To show the complementary information provided by the miniature probe, we prepared a phantom consisting of a 700-µm plastic tube with air inside, a 700-µm plastic tube with ink filled inside, a 200-µm black bristle, a 225-µm glass fiber, and a 100-µm steel line, which are labeled as 1–5, respectively, in Fig. 7(a), where the relative positions of the objects are also illustrated. The crosstalk removal algorithm and SAFT are applied, and Hilbert transform is further used along the z direction to acquire the signal envelope. Figures 7(b) and 7(c) shows PA and US images, respectively, with suitable dynamic ranges for better visualization. The fused PA and US image is shown in Fig. 7(d), demonstrating the capability of our probe in acquiring dual contrasts. In Fig. 7(b), the PA image can only visualize objects 2 and 3 because only the ink and the black bristle have prominent light-absorbing characteristics. On the other hand, in Fig. 7(c), the US image is able to reveal all objects 1–5, although objects 2, 3, and 5 have relatively low image intensity. This is because the objects 1 and 4 have relatively stronger acoustic impedance mismatch between the materials and water than objects 2, 3, and 5. Furthermore, we are able to simultaneously observe the top layer of object 2 (the plastic tube) by US imaging and the ink inside by PA imaging, as indicated in Fig. 7(d).

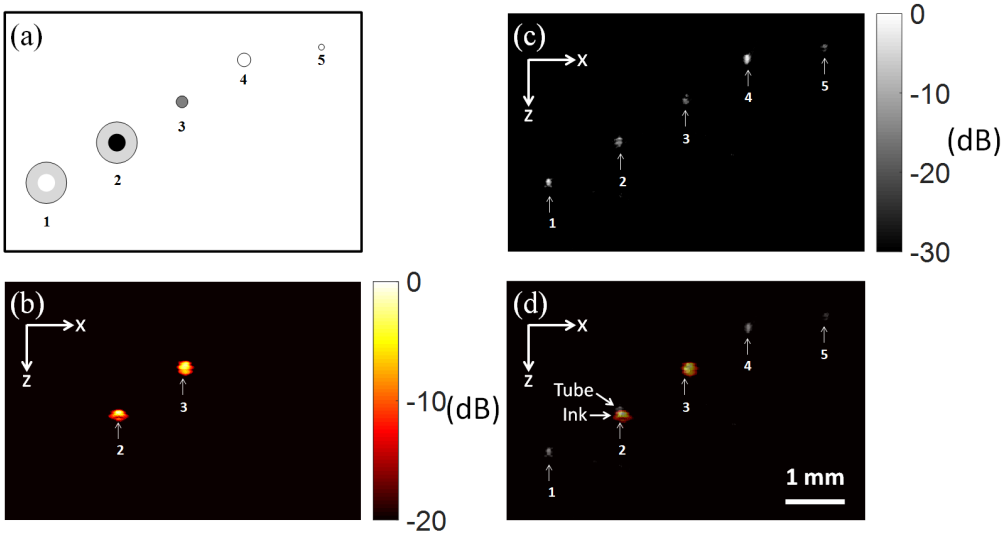

Fig. 7. (a) Illustration of the phantom consisting of a 700-µm plastic tube with air inside, a 700-µm plastic tube with ink filled inside, a 200-µm black bristle, a 225-µm glass fiber, and a 100-µm steel line, which are labeled as 1–5, respectively. (b) PA image with peak SNRs of 70 and 68 dB for objects 2 and 3, respectively. (c) US image with peak SNRs of 65, 58, 52, 65, 49 dB for objects 1–5, respectively. (d) PA-US fused image. The 1 mm scale bar is for images (b)–(d).

Optics EXPRESS

3.3 Three-dimensional phantom imaging

To further evaluate the capability of the dual-modality probe for three-dimensional (3D) imaging, a 200-µm black bristle and a 250-µm steel line, both with knotted structures, were imaged. Two-dimensional (2D) PA SAFT and 2D US SAFT are employed for image formation. Figures 8(a) and 8(b) show the PA and US maximum amplitude projection (MAP) along the depth direction, respectively. Figures 8(c) and 8(d) show the 3D volumetric PA and US images, respectively. As indicated by the above result of the 2D phantom imaging, the black bristle has both PA and US contrasts while the steel line has US contrast alone. Thus, both the black bristle and the steel line can be observed by the US image while only the former is revealed by the PA image, as shown in Fig. 8. Besides, the knotted structures can be clearly visualized by both PA and US imaging, demonstrating the high-resolution capability of our probe.

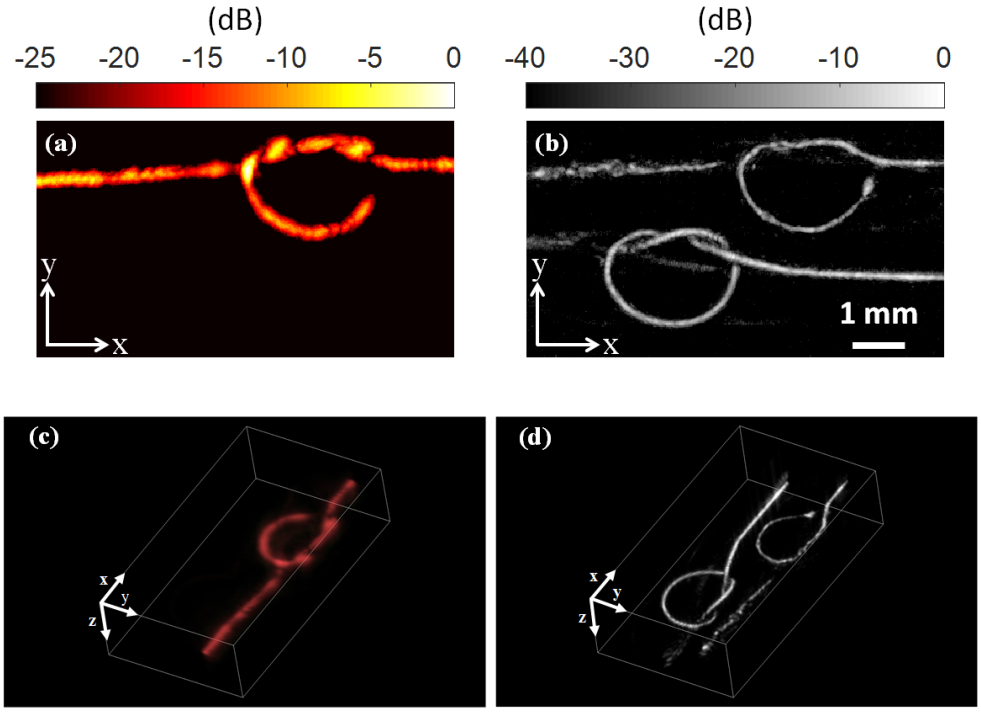

Fig. 8. PA and US images of a phantom consisting of a 200-µm black bristle and a 250-µm steel line, both with knotted structures. Image dimensions: 8 mm × 4.5 mm × 2 mm along x, y, and z axis, respectively. (a) PA MAP image on the x-y plane with a peak SNR of 62 dB. (b) US MAP image on the x-y plane with peak SNRs of 50 and 53 dB for the black bristle and the steel line, respectively. The 1 mm scale bar is for images (a) and (b). (c) 3D volume rendering PA image. (d) 3D volume rendering US image. 3D animations are available as supplementary videos: 3D volume rendering PA image (see Visualization 1) and US image (see Visualization 2).

4. Discussion

To show the prominent progress of this work, we compare the performance of our probe with that of other miniature PA-US probes in Table 1. In this work, we aim to construct a miniature probe capable of not only high PA and US lateral resolutions but high PA and US resolutions over a large imaging depth range. Thus, several works are excluded from the comparison in Table 1. First, the work employing optical-resolution PA endoscopy (e.g., [10]) is excluded because it can provide high PA lateral resolution (10–20 µm) but only within a limited imaging depth (~1 mm). Second, the works with external light illumination

Optics EXPRESS

[12–14] are excluded because the probe should be further developed before it can be used for intravascular imaging. Moreover, after integrating an additional component to realize internal light illumination, the probe size, lateral resolutions, and imaging depth range are subject to change. Third, the works with only PA modality or only US modality [18] are excluded.

Table 1. Comparison of lateral/transverse resolution and imaging depth range of miniature PA-US probes

Probe design	Acoustic detection technology	Lateral/transverse resolution (μm)	Imaging depth range (mm)	Probe diameter (mm)	Refs.
An angle-polished optical fiber (PA excitation) adjacent to an US transducer (US generation and acoustic detection)	Piezoelectric transducer	500–1000 (PA and US)[a]	> 5	1–2	[3,11,16]
An optical fiber (PA excitation) and a ring US transducer (US generation and acoustic detection)	Piezoelectric transducer	230–480 (PA); NA for US	> 2.6	2.3	[17]
An optical fiber with a cone-shaped mirror (PA excitation), a ring-shaped transducer (sideward US generation), and a microring sensor (acoustic detection)	Microring sensor	NA[b]	NA	3	[15]
Three optical fibers for PA excitation, US generation, and acoustic detection; large-NA SAFT is used.	FP sensor	104–154 (PA); 64–112 (US)	> 4	< 2	This work

[a]Estimated by the diameter of the US transducers [16]. [b]Not calibrated. Based on the imaging mechanism by this design [15], the resolution is supposed to be poor.

As can be seen, our probe achieves by far the best performance in terms of lateral resolutions and imaging depth range. This is made possible by the unique probe design that enables large-NA SAFT for PA and US imaging through wide-angle PA excitation, US generation, and acoustic detection. Note that the existing works with a similar design using two or three optical fibers either demonstrated only US modality [18,21] or did not make special efforts to facilitate large-NA SAFT to show high resolutions [22]. Although an all-optical scanhead employing SAFT for PA and US imaging was presented, neither definite miniaturization of the scanhead nor detailed calibration of PA and US resolutions at different depths was demonstrated [19,20].

As mentioned, we intend to build a miniature probe for endoscopic and intravascular imaging applications with both high resolutions and a large imaging depth range. Focusing the optical (excitation) and/or acoustic beam (transmission and/or detection) is an alternative approach to achieve high resolution. However, such focusing has issues: (1) Optical beam focusing (excitation) can be achieved by using a large-NA optical lens, but high PA resolutions are guaranteed only within limited depth of focus. Moreover, the overall size of the probe due to the optical lens may become big, which is not desired for building a miniature probe. (2) Acoustic beam focusing (transmission and/or detection) can be realized by using a large-NA transducer or an acoustic lens, but has similar issues of limited depth of focus and possibly big size. Thus, a "digital" focusing by SAFT is employed in this work, which allows both miniaturization of the probe and high resolutions over a large imaging depth range. To realize large-NA SAFT, wide-angle excitation/transmission and detection are both needed.

In the PA resolution calibration, the imaged size of 72–117 μm (axial) is slightly smaller than the target of 90-μm human hairs. This might be due to non-uniform light absorption and thus, effectively, a smaller PA target size [38]. In the US resolution calibration, the imaged size of 64–112 μm (lateral) and 31–67 (axial) is smaller than the target of 125-μm glass fibers, which may be explained below. US imaging is to detect the boundary of the glass fiber (not the whole glass fiber itself). Moreover, in the calibration, the detected US signals mainly come from acoustic reflection (in contrast to acoustic scattering) because of the round target.

Optics EXPRESS

In such a scenario, only part of the top boundary will be imaged. That is, the effective US target size is smaller than the glass fiber itself.

The fiber FP sensor used in our PA-US probe currently has an NEP of 0.4 kPa. As mentioned above, it is possible to improve the sensitivity of the current fiber FP sensor by up to 50 times [29]. In this regard, the imaging sensitivity of the proposed PA-US probe demonstrated in this work can be significantly improved.

Currently, we perform linear scanning to prove that our probe is capable of high resolutions over a large depth range. For IVPA and IVUS imaging applications, further development is needed. First, a micromotor and a rod mirror can be integrated to realize circular scanning and side-viewing imaging, which is technically feasible [39]. Second, circular SAFT can be used to obtain high transverse resolutions over a large imaging depth range along the radial direction given the optimized probe design [37]. Thus, the PA-US probe demonstrated in this work can be further developed to facilitate IVPA and IVUS imaging with potential to achieve high resolutions and a large imaging depth range.

In this work, we acquire PA and US imaging separately. To perform PA and US imaging simultaneously, one method is coupling the light to the PA and US fibers concurrently and separating PA and US waves at different time periods in one A-line signal detected by the FP sensor given suitable imaging range, as detailed in [8]. Another method is sequential excitation of PA and US waves (i.e., PA, US, PA, US…) with a proper time delay so that the FP sensor can differentiate the two waves.

5. Conclusions

In summary, we construct an all-optical miniature probe capable of dual-modality PA-US imaging and achieve high resolutions over a large imaging depth range via a large synthetic aperture for numerical focusing. The miniature probe consists of three optical fibers. The first is the large-NA multi-mode fiber for wide-angle laser illumination. The second is the multi-mode fiber coated with the carbon black-PDMS composite film for wide-angle US transmission. The third is the single-mode fiber with the FP optical cavity on the fiber end face for detecting acoustic waves. The FP sensor is able for broadband and wide-angle acoustic detection. The synergy of the three fibers allows large-NA PA and US SAFT so that high resolutions over a large depth range of both PA and US imaging modalities can be achieved. The outer diameter of the probe is ~2 mm, which can be used for not only endoscopic but also intravascular applications with complementary PA and US contrasts. The phantom imaging shows the ability of the probe to acquire the complementary PA and US contrasts. Imaging of biological tissue using the miniature probe is of great interest for future work. Development of the fiber-tip FP sensor with broader bandwidth (e.g., > 50 MHz) is essential to further enhance the spatial resolutions in both PA and US imaging.

Funding

National Natural Science Foundation of China (NSFC) (61405112); National High Technology Research and Development Program of China (863 Program) (2015AA020944); Shanghai Science and Technology Committee (STCSM) (15140901400).